

Performance Analysis and Validation of a Stereo Vision System

Won S. Kim, Adnan I. Ansar, Robert D. Steele, and Robert C. Steinke

Jet Propulsion Laboratory
California Institute of Technology
4800 Oak Grove Drive, Pasadena, CA 91109-8099, USA
Won.S.Kim@jpl.nasa.gov

Abstract – *This paper presents an in-depth performance analysis and validation of a correlation based stereo vision system being used as part of the ongoing 2003 Mars Exploration Rover flight mission. Our analysis includes the effects of correlation window size, pyramidal image down-sampling, vertical misalignment, focus, maximum disparity, stereo baseline, and range ripples. A key element of validation is to determine the stereo localization error both analytically and experimentally. We study both down-range and cross-range error and verify that while camera calibration inaccuracy contributes to both, correlation error affects only the former. Error contributions of subpixel interpolation, vertical misalignment, and foreshortening on stereo correlation are examined carefully. A novel method using bricks with reflective metrology targets and a mast-mounted stereo camera system enabled experimental measurements of the stereo disparity error. The standard deviation of the down-range disparity error was measured at $\sigma=0.32$ pixel for high-resolution 1024×768 camera images. The result is critical in evaluating accurate rover navigation and instrument placement within given error budgets.*

Keywords: Stereo vision, stereo localization error, stereo correlation, subpixel interpolation, foreshortening.

1 Introduction

A binocular stereo vision system generates a 3D reconstruction of points imaged by a pair of cameras using their associated camera models. A catalog of stereo techniques along with performance characteristics is presented in [1]. An extensive bibliography of various aspects of stereo vision is listed in [2]. In this paper we focus our analysis and experimental validation on a particular stereo vision system – the JPL (Jet Propulsion Laboratory) stereo vision software module [3], which is being used for the 2003 Mars Exploration Rover (MER) flight mission. In particular, we performed an extensive stereo localization error analysis, more complete than that presented in an earlier paper [4]. By employing a novel method of using bricks with reflective metrology targets and a mast-mounted stereo camera system, we obtained experimental measurements of the stereo disparity subpixel error successfully. We used the CLARATy (Coupled Layer

Architecture for Robotic Autonomy) stereo vision package to run JPL Stereo within the CLARATy testbed. CLARATy [5] provides a common software environment that enables comprehensive control for planetary rovers and robotic systems. The validation process is an important part of an error budget analysis of rover-stereo-based navigation and instrument placement. We anticipate that the analysis and experimental validation presented here will be applicable to other correlation based stereo systems as well.

After a brief description of the JPL Stereo Vision software in Section 2, we present an in-depth performance analysis of JPL Stereo in Section 3, stereo localization error analysis in Section 4, and experimental validation in Section 5.

2 JPL Stereo Vision Software

Figure 1 shows a functional diagram of the JPL stereo vision software. We briefly review the steps. Rectification refers to virtual realignment of the stereo image pair to guarantee that matching pixels occur on the same scan lines in both images. This reduces matching to a 1D search instead of 2D. Pyramidal reduction is a factor of 2^n ($n \geq 0$) image size reduction, depending on desired range resolution. Difference of Gaussians refers to a convolution of the image with a filter comprised of the difference of two Gaussian kernels. This amounts to a bandpass filter and is used to compensate for photometric variations between the cameras of the stereo pair. Correlation is the process of matching pixels between image pairs using a local similarity metric, in our case the sum of absolute differences (SAD) of image intensity values in a neighborhood of the pixels being matched. Blob filtering refers to the removal of small patches of incongruous data to produce a coherent disparity map. Integer disparities are converted to subpixel values by interpolation of correlation scores and then to a range map via triangulation. Additional detail together with the CLARATy API can be found in the Stereo Vision Technology Functional Design Document [6]. JPL Stereo emphasizes accurate range results with a high percentage of valid range data, while maintaining reasonable computational time and cost. The density of range data is important for reliability, while range accuracy is important for accurate rover navigation and instrument placement within given error budgets.

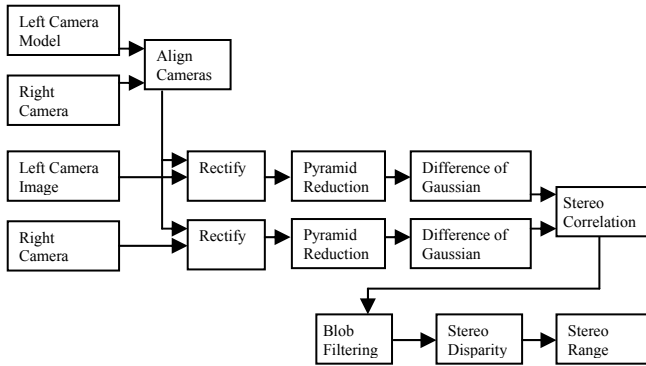


Figure 1. functional diagram of JPL stereo vision software

3 Stereo Vision Performance

Extensive tests and validation of the JPL camera calibration and stereo vision technology were performed and described in a detailed report [7]. A concise summary of the relevant findings is presented in Sections 3 and 4.

3.1 Correlation window size

Correlation window size affects stereo correlation performance. Too large or too small a window size yields a poor range. In general, a densely textured scene, such as a rocky terrain, performs better with a smaller window size (e.g., 7×7 or 9×9 pixels), while a sparsely textured scene, such as a sand dune, usually works better with a larger window size (e.g., 15×15 or 29×29 pixels). The "foreground fattening" effect, in which a textured foreground tends to be fattened over a less-textured background, is more conspicuous for wider windows.

3.2 Pyramidal image down sampling

Pyramid reduction downsamples the image by a factor of 2 at each succeeding pyramid level by averaging over 2×2 blocks of pixels. Thus, a pyramid level of n corresponds to a size reduction by 2^n . Each successive pyramid level reduces the computational time for stereo correlation by a factor of 8. Lower resolution makes stereo correlation less sensitive to focus and camera calibration errors at the expense of 3D range accuracy and resolution.

3.3 Vertical misalignment

The stereo algorithm performs a one-dimensional search assuming rectified left and right images are well aligned vertically. This alignment relies on the accuracy of the camera models. To test the effect of vertical misalignment we shifted one image of a pair vertically and measured the percentage of valid disparity pixels.

Experimental results (Figure 2) show that noticeable degradation of the stereo correlation performance starts at about ± 0.5 pixel vertical misalignment, where the percentage of valid disparity pixels is reduced by 13%, from the maximum 86% to 75%. At ± 1 pixel vertical

misalignment, the percentage is reduced by 50%. Pyramid reduction makes correlation less sensitive to vertical misalignment. Increasing the pyramid level by 1 reduces the sensitivity by a factor of 2. For the pyramid level 1 (Figure 2), the percentage of valid disparity pixels starts to degrade rapidly beyond the ± 1 pixel vertical misalignment. Vertical misalignment also contributes to stereo disparity error (see Section 3).

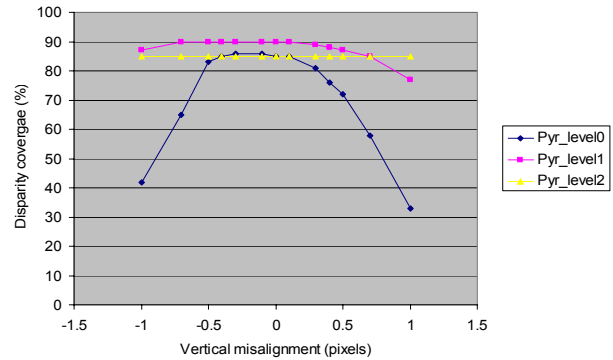


Figure 2. Effect of vertical image shift on the percentage of valid disparity pixels

3.4 Focus

Good camera focus is vital to stereo performance. We found this to be especially true for narrow field of view cameras, which are mechanically very sensitive to focal adjustment. To evaluate the effect of defocus, we blurred one image of a stereo pair with a Gaussian filter, and measured the percentage of valid disparities. In Figure 3, the left camera image is well-focused, while the right camera image is not. The stereo correlation of this pair at full resolution resulted in an empty or 0% disparity map (Figure 4). When the left image was blurred by using a Gaussian filter with $\sigma = 1.5$ pixel, the percentage of valid disparity pixels reached the maximum (Figure 4). The stereo correlation starts to degrade rapidly outside the range $1 < \sigma < 2$, a range of ± 0.5 pixel. Stereo matching at lower resolution using a higher pyramid level is less sensitive to focus mismatch. At half resolution (pyramid level = 1), rapid degradation occurs outside the range $0.5 < \sigma < 2.5$ (a range of ± 1 pixel), a window twice as wide. At one quarter resolution (pyramid level = 2) the effect of the poorly focused right image is largely unnoticeable.

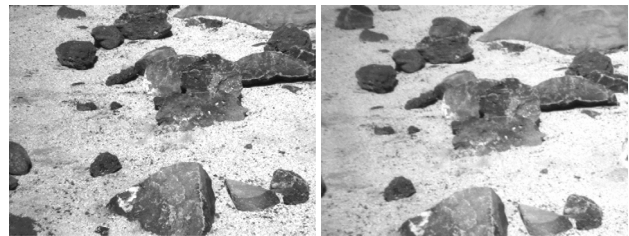


Figure 3. A well-focused left camera image (left) and a slightly out-of-focus right camera image (right)

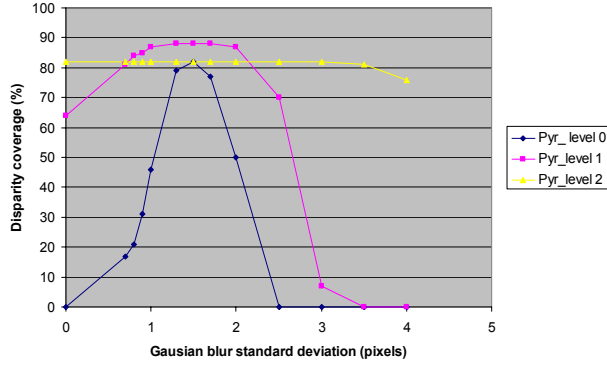


Figure 4. Effect of image defocus on stereo correlation; the left camera is blurred to match with the right camera.

3.5 Maximum disparity

The algorithm to find pixel correlation searches from a specified minimum to maximum disparity value. From (2) of Section 3, the maximum disparity d_{max} determines the minimum stereo range Z_{min} (more correctly, minimum stereo z-axis distance) by

$$Z_{min} = f B / d_{max} = (f_l / q) B / d_{max} , \quad (1)$$

where B is the stereo baseline, f_l and f are the camera's focal length in mm and pixels, respectively, and q is the pixel size in mm. As an example, we used a Point Grey Research Dragonfly digital camera equipped with a Sony ICX204AL 1/3-in CCD image sensor of 1024×768 pixels resolution. Since the image size of the 1/3-inch format CCD is approximately 4.8×3.6 mm, we can estimate the pixel size as 4.8/1024=4.69 μ m. Its actual pixel size according to the manufacture's specification is 4.65×4.65 μ m, or $q=0.00465$ mm. For 16-mm lenses (17°×13° field of view) and a 0.3 m stereo baseline, the minimum stereo range is 4 m when $d_{max}=256$ pixels, and 2 m when $d_{max}=512$ pixels.

3.6 Stereo baseline

Increasing the stereo baseline reduces the range error. However, it increases the stereo minimum range as related by (1), limiting the closest object that can be found. It also reduces the percentage of valid disparity pixels for two reasons. First, the image overlap becomes smaller as the baseline increases. Second, the viewpoint difference between left and right cameras increases, causing projected images to vary more in shapes and introducing more occlusions, thus making matching more difficult.

3.7 Range ripples

The "ripple effect" is shown in Figure 5. Range ripples form a pattern of lines perpendicular to the optical axis. Figure 5 is an enlarged view of part of a disparity histogram showing the number of range points detected at subpixel disparities of 0.1 pixel steps. The maximums occur at integer-pixel disparities while minimums occur at

half-pixel disparities. This effect is consistent over the entire range. There are two contributing factors. The correlator has more difficulty in finding matches at half-pixel disparities, and matches at quarter-pixel disparities are biased towards the nearest integer (see Section 4.4). The relation (2) of Section 3 explains why the ripples form a pattern of parallel lines rather than concentric circles. The disparity d is proportional to the z-axis distance Z . Each ripple peak occurring at an integer disparity is made of points that have the same z-coordinate value.

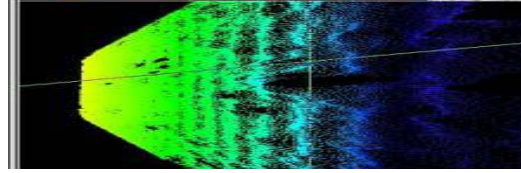


Figure 5. A stereo range map viewed from overhead, showing the ripple effect

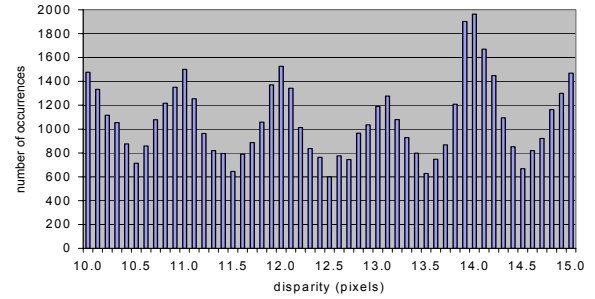


Figure 6. Portion of the disparity histogram

4 Stereo Localization Error Analysis

4.1 Stereo Localization Geometry

We now derive the relationship of the disparity error to the stereo 3D localization error. Figure 7 shows the localization geometry with a stereo camera pair. By similar triangles, the disparity d and the z-axis (along the optical axis) distance Z are related by

$$Z = f B / d , \quad (2)$$

where B is the stereo baseline, and f is the camera's focal length in pixels. This equation implies that constant disparity d corresponds to a fronto-parallel plane, not a sphere. In Figure 6, the plane will show up as a line parallel to the x-axis. Differentiating (2) and then substituting fB/Z for d , we get

$$\Delta Z = -(Z^2 / f B) \Delta d , \quad (3)$$

This relation can also be obtained geometrically from Figure 7. The negative sign appears because Z decreases as d increases. Since $Z = R \cos \theta$ and $\Delta Z = \Delta R \cos \theta$,

$$\Delta R = -(R^2 \cos \theta / f B) \Delta d , \quad (4)$$

$$|\Delta R| \cong (R^2 / f B) |\Delta d| , \quad (5)$$

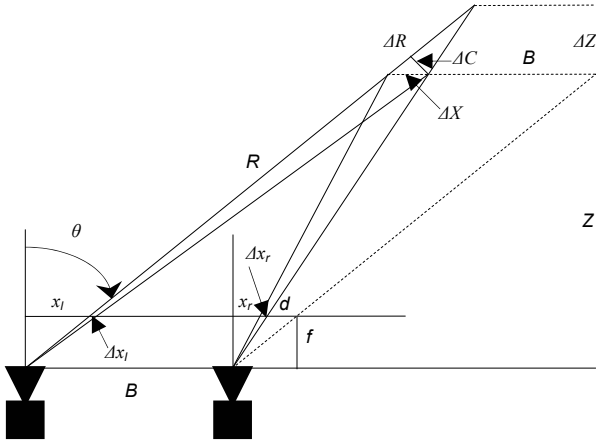


Figure 7. Geometry of stereo localization

The down-range error ΔR is along the line of sight, where Δd is added for the right image only in Figure 7 ($\Delta x_l = 0$; $\Delta x_r = \Delta d$). For the cross-range error that is perpendicular to the line of sight, we consider adding Δx for both left and right image points ($\Delta x_l = \Delta x_r = \Delta x$). By similar triangles,

$$\Delta X = (Z/f) \Delta x. \quad (6)$$

Since $\Delta C = \Delta X \cos \theta$,

$$\Delta C = (R \cos^2 \theta / f) \Delta x, \quad (7)$$

$$\Delta C \cong (R/f) \Delta x. \quad (8)$$

Now we consider a general case when both Δx_l and Δx_r are nonzero. Since $d = x_l - x_r$, and $\Delta d = \Delta x_l - \Delta x_r$, from (5)

$$|\Delta R| \cong (R^2 / f B) |\Delta x_l - \Delta x_r|, \quad (9)$$

The stereo down-range error is directly related to the difference of Δx_l and Δx_r . On the other hand, the common average error $(\Delta x_l + \Delta x_r)/2$ changes neither the disparity nor the down-range error. It only affects the stereo cross-range error. From (8),

$$\Delta C \cong (R/f) (\Delta x_l + \Delta x_r)/2, \quad (10)$$

From (9) and (10), the standard deviations of the errors are related by

$$\sigma_{\Delta R} \cong (R^2 / f B) \sigma_{\Delta d} = (R^2 / f B) \sigma_{\Delta x_l - \Delta x_r}, \quad (11)$$

$$\sigma_{\Delta C} \cong (R/f) \sigma_{(\Delta x_l + \Delta x_r)/2}. \quad (12)$$

In general, the stereo localization error is described by an error ellipsoid in 3D space bounded by the down-range and cross-range errors of (11) and (12). The down-range error increases as the square of the range while the cross-range error does so linearly. As the range increases, the down-range error along the line of sight is dominant as can be observed in a stereo range 3D visualization of Figure 8.

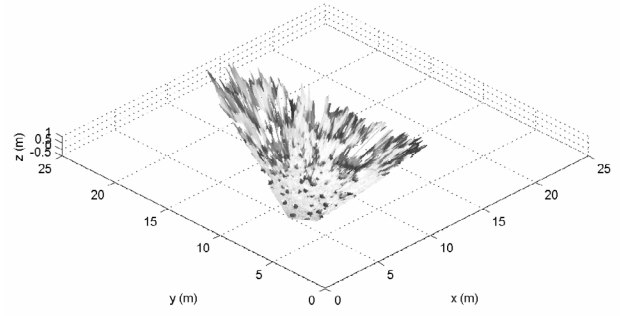


Figure 8. Visualization of stereo range 3D data

Camera calibration inaccuracy (including mast calibration inaccuracy for mast-mounted cameras) affects both stereo down-range and cross-range errors, while stereo correlation inaccuracy affects the down-range error only.

4.2 Camera calibration inaccuracy

The error model of (11) and (12) can be tested by using camera calibration data. Since the camera calibration process produces the 3D metrology of the calibration fiducials (dots in Figure 9) as well as their associated 2D image points, we can compute both 2D reprojection error and the 3D localization error.

The 2D reprojection error was obtained by comparing the 2D projections of the metrology-based 3D positions of calibration dots and their corresponding 2D image points. For a stereo image pair tested using 2.3 mm lenses ($113^\circ \times 86^\circ$ field of view), the 2D reprojection differential and common errors were $\sigma_{\Delta x_l - \Delta x_r} = 0.12$ pixel and $\sigma_{(\Delta x_l + \Delta x_r)/2}$

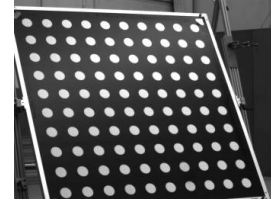


Figure 9. A 10x10 dots camera calibration target image

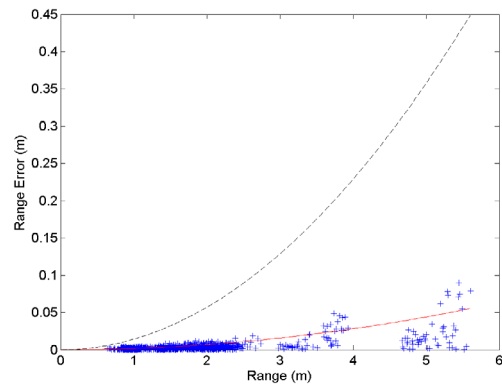


Figure 10. Down-range error caused by camera calibration inaccuracy; $\sigma_{\Delta x_l - \Delta x_r} = 0.12$ pixel (red) and 1 pixel (black)

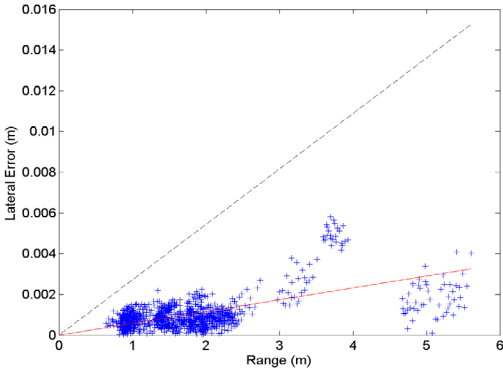


Figure 11. Cross-range error caused by camera calibration inaccuracy; $\sigma_{(\Delta x_l + \Delta x_r)/2} = 0.21$ pixel (red) and 1 pixel (black)

$= 0.21$ pixel, respectively. Using these values, the down-range and cross-range error models of (11) and (12) are plotted with red solid lines in Figures 10 and 11. The 3D localization error for each calibration dot, which is computed by comparing the metrology-based 3D position and the stereo range 3D position constructed from the 2D image point pair based on the stereo camera models, is also plotted with a '+' mark in Figures 10 and 11. The measured 3D localization error values agree well with the expected error model predicted by (11) and (12).

4.3 Stereo correlation inaccuracy

Stereo correlation performance is affected by various factors including subpixel interpolation, vertical misalignment, and foreshortening. Some of the details are described here.

4.4 Subpixel interpolation

The JPL stereo correlation employs quadratic subpixel disparity interpolation, in which correlation scores at three adjacent disparity values are used to estimate the disparity value to subpixel accuracy. This interpolation improves the accuracy of the stereo disparity estimate, but still yields some inaccuracy. To evaluate this inaccuracy, we shifted an image by an integer plus some subpixel amount (Figure 12), and compared the stereo correlator output disparity with the actual image shift. The horizontal image shift corresponds to the case where a fronto-parallel planar surface moves back or forth. If the stereo correlator were perfect, every pixel would register a disparity equal to the actual amount of the shift. By observing deviations from the correct disparity, we can estimate the amount of subpixel error introduced by the stereo correlator subpixel interpolation.

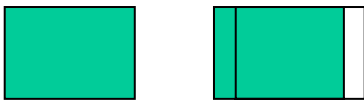


Figure 12. Horizontal image shift corresponds to the case when a fronto-parallel planar surface moves back or forth.

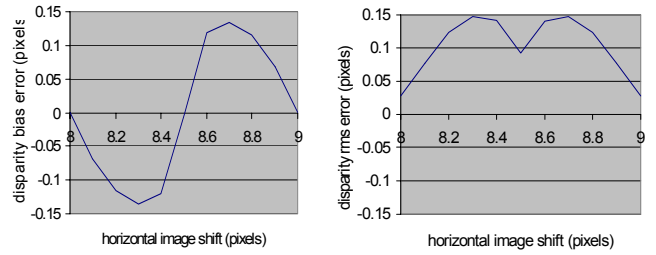


Figure 13. Disparity bias error (left) and rms error (right) of the subpixel disparity interpolation, obtained by varying the amount of horizontal image shift.

The results (Figure 13 left side) indicate that the subpixel quadratic interpolation has a bias error in estimating the subpixel disparity value. The bias tends towards the nearest integer disparity, and is about 0 at half integer disparities. Due to a large bias value at quarter integer disparities, the rms disparity error relative to the actual horizontal image shift yields double humps (Figure 13 right side) at integer+0.25 and integer+0.75 pixels. The stereo disparity rms error due to subpixel interpolation can be computed as the disparity rms error over all integer and fractional disparities, or $\sigma_{\Delta d, interpol} = 0.11$ pixel.

4.5 Vertical misalignment

Vertical misalignment caused by imperfect camera calibration also affects the stereo performance. To investigate the effect of vertical misalignment, the left image is shifted both horizontally and vertically (Figure 14). Figure 15 shows the bias and rms errors of the stereo disparity estimate for various vertical disparities. The

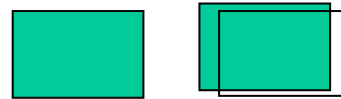


Figure 14. A horizontal & vertical image shift corresponds to the case when a fronto-parallel planar surface moves back or forth with a vertical misalignment

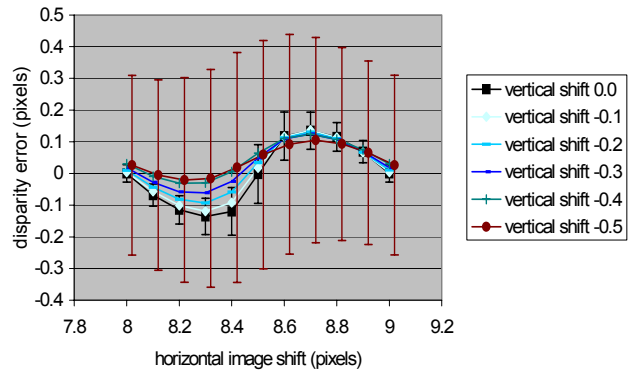


Figure 15. Stereo disparity error over horizontal and vertical image shifts

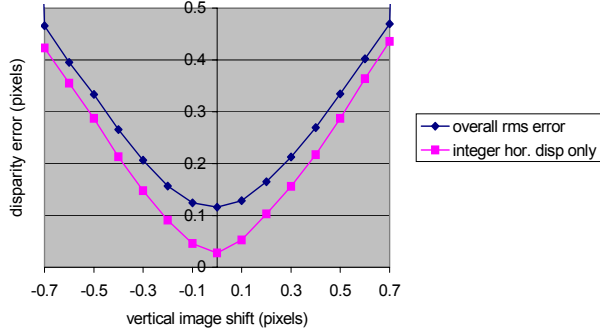


Figure 16. Stereo disparity rms error due to vertical misalignment (vertical image shift) and subpixel interpolation (horizontal image shift)

curves show mean deviation, and the vertical bars show standard deviation from the mean for 0.0 to -0.5 pixel vertical shifts. Horizontal shifts of 8.1-8.4 pixels have a negative mean deviation, biased towards 8 pixels, while horizontal shifts of 8.6-8.9 pixels have a positive mean deviation, biased towards 9 pixels. Vertical shift reduces the mean bias error somewhat, but increases the rms error. The stereo disparity rms error caused by only vertical misalignment can be computed by considering only integer horizontal image shifts (Figure 16, red square marks), while the stereo disparity error caused by both subpixel interpolation and vertical misalignment can be computed by considering all horizontal image shifts of both integer and fractional values (Figure 16, blue diamond marks). The two curves in Figure 16 suggest that the stereo disparity rms error due to vertical and horizontal image shift can be approximately decoupled,

$$\sigma_{\Delta d, combined}^2 \cong \sigma_{\Delta d, interpol}^2 + \sigma_{\Delta d, vertical_misalign}^2, \quad (12)$$

where $\sigma_{\Delta d, interpol} = 0.11$ pixel from Section 4.3.

4.6 Foreshortening

Foreshortening error also contributes to the stereo disparity error [4]. When a planar surface tilts forward or backward, the left and right images are related by a shear (Figure 17). It can be shown that

$$x_{R,i} = x_{L,i} - (f B / Z_0) + (m_x B / Z_0) y_i, \quad (14)$$

where m_x is the surface tilt slope relative to the vertical plane and $m_x B / Z_0$ is the disparity increment rate per row on the right image. With the baseline $B = 0.2$ m, the disparity



Figure 17. Image shear corresponds to the case when the planar surface is tilted forward or backward.

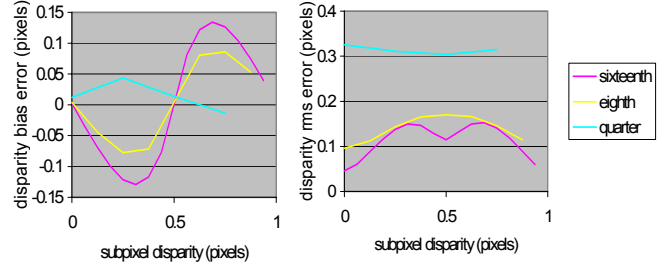


Figure 18. Disparity bias error (left) and rms error (right) of the subpixel disparity interpolation, obtained by varying the image shear rate of 1/4, 1/8, 1/16 pixel shift per row

increment rate becomes 1/8 pixel per row, when the surface horizontal slope relative to the horizontal plane = 9° at 10 m away, 39° at 2 m, or 58° at 1 m. Figure 18 shows the stereo disparity bias and rms errors for three different image shear rates with a window size of 9×9 pixels. The results are similar to Figure 13 for the horizontal image shift.

When a planar surface rotates left or right from the fronto-parallel vertical plane, it also introduces foreshortening error. This time it has an effect of causing stretching or squeezing the left image to get the right image (Figure 19). It can be shown that

$$x_{R,i} = x_{L,i} - (f B / Z_0) + (m_y B / Z_0) x_i, \quad (14)$$

where m_y is the surface rotation slope relative to the vertical plane and $m_y B / Z_0$ is the disparity increment rate per column on the right image. Figure 20 shows the stereo disparity bias and rms errors for three different image rotation rate with the window size of 9×9 pixels. The results are very similar to Figure 17 for the image shear, except that the rms error values are slightly larger.



Figure 19. Image stretch/squeeze corresponds to the case when the planar surface is rotated sideways

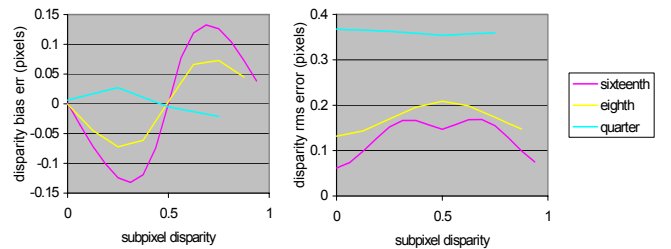


Figure 20. Disparity bias error (left) and rms error (right) of the subpixel disparity interpolation, obtained by varying

the image stretch rate of 1/4, 1/8, 1/16 pixel shift per column

4.7 Computing Overall Localization Errors

So far we examined various sources contributing to the stereo localization error individually. Now we tally all of these individual errors and compute the combined error. Noting that down-range and cross-range errors can be computed by (11) and (12) for the given range, all we need to determine is the overall stereo disparity error $\sigma_{\Delta d}$ and the common horizontal reprojection error $\sigma_{(\Delta x_l + \Delta x_r)/2}$ in pixels. We analyzed the stereo localization error for five different stereo settings: three (2.3mm, 4 mm, 16 mm focal length lenses) with total station metrology and two (2.8 mm and 16 mm) with laser tracker metrology. The metrology accuracy was 1/100,000, or 0.1 mm over a 10 m range for the laser tracker (Leica LTD 500) and 0.5 mm for the total station (Leica TDM 5000).

Table 1 shows the 2D reprojection errors of the five stereo cameras. Rows 3-4 (yellow) are the camera calibration residual rms errors between the 2D image points of the calibration dots and the 2D reprojections of the corresponding 3D positions obtained from metrology. Rows 5-7 (green) are 2D reprojection errors between right and left camera calibration dots: vertical alignment error in row 5, common horizontal reprojection error in row 6, and differential horizontal error in row 7. The common horizontal reprojection errors of row 6 solely determine the stereo cross-range errors by (12). Rows 8-11 (blue) are stereo disparity error components contributed by stereo correlation inaccuracy. The stereo disparity errors due to vertical misalignment (row 8) were obtained by using Figure 16 red curves and vertical misalignment data of row 5. The stereo disparity error due to subpixel disparity interpolation (row 9) was assumed 0.11 pixel (see Section 4.4) for all stereo cameras. The error due to image shear (row 10) was assumed 0.07 pixel, and the error due to image squeeze (row 11) was assumed 0.11 pixel (see Section 4.6).

The overall disparity error (grey) for the fronto-parallel surface of a rock (row 12) can be computed by the RSS (root-sum-squared) values of the range disparity errors from the three different sources of camera calibration, vertical misalignment, and subpixel disparity interpolation. For the top and side surfaces of the rock (rows 13 and 14, respectively), the RSS computation of the overall stereo disparity error needs to include an additional error due to foreshortening image distortion: image shear for the top surface and image stretch/squeeze for the side surface. From rows 12-14, the average of the overall stereo disparity errors is 0.24 pixels for total station metrology, while 0.17 pixels for laser tracker metrology. The laser tracker metrology thus reduces the overall disparity error by 0.07 pixel or 29%. For both laser tracker and total station metrologies, 1σ of the stereo disparity error was less than 1/3 pixel, and 3σ was less than 1 pixel.

Table 1. Stereo localization error computations

Metrology	Total Station			Laser Tracker	
	Lens	2.3mm	4mm	16mm	2.8mm
left cam residual error	0.42	0.62	0.45	0.19	0.29
right cam residual error	0.43	0.63	0.42	0.20	0.29
vertical misalignment	0.11	0.15	0.31	0.07	0.07
$\sigma_{(\Delta x_l + \Delta x_r)/2}$	0.29	0.54	0.19	0.14	0.19
$\sigma_{\Delta d}$ camcal	0.15	0.18	0.17	0.11	0.09
$\sigma_{\Delta d}$ vert-misalignment	0.06	0.07	0.16	0.04	0.04
$\sigma_{\Delta d}$ subpixel-interpol	0.11	0.11	0.11	0.11	0.11
$\sigma_{\Delta d}$ shear	0.07	0.07	0.07	0.07	0.07
$\sigma_{\Delta d}$ stretch-squeeze	0.11	0.11	0.11	0.11	0.11
$\sigma_{\Delta d}$ for fronto-parallel	0.20	0.22	0.26	0.16	0.15
$\sigma_{\Delta d}$ for top of rock	0.21	0.23	0.27	0.18	0.16
$\sigma_{\Delta d}$ for side of rock	0.22	0.25	0.28	0.19	0.18

5 Stereo Range Error Measurements

As a way to measure the stereo range error accurately, we used bricks with reflective-tape targets attached to the four corners (Figure 21). This had two primary benefits: 1) it enabled us to measure accurate 3D positions of reflective-tape targets with a total station, and 2) it reduced ambiguity in human mouse-click entry of corresponding target points in left and right camera images. In the experiment, we placed a dozen bricks from 1 to 14 m away from the Navcam stereo camera system with 6 mm lenses ($49^\circ \times 37^\circ$ field of view) mounted on a rover pan-tilt mast. We collected camera images with different mast tilt angles from -0.1° to -0.8° . We recorded the tilt angles for appropriate range data transformations based on mast calibration [8]. We also measured reflective-tape target 3D positions using a Leica TCRA 1103 total station with 2 mm accuracy. Note that this accuracy is not as good as the accuracies of the surveying equipment used in Section 4.7 and Table 1.

After the data collection, we gathered the corresponding left and right image positions of the reflective-tape targets using two methods: 1) human integer-pixel matching by manual mouse-clicking and 2) stereo subpixel correlation matching. Since the mouse-click entry accepts only integer values, mouse clicking inherently has ± 1 pixel quantization error. On the other hand, subpixel correlation matching enables subpixel accuracy. Down-range disparity error in Figure 22 was 0.54 pixel with human integer-pixel matching and 0.32 pixel with stereo subpixel correlation matching. The improvement realized by using subpixel matching over integer-pixel matching is significant. Cross-range disparity error (Figure 23) was 1.36 pixels with human integer-pixel matching, and 1.39 pixels with stereo subpixel correlation matching. As expected, subpixel correlation does not improve cross-range disparity error.



Figure 21. Bricks with reflective targets were used for stereo range error measurements

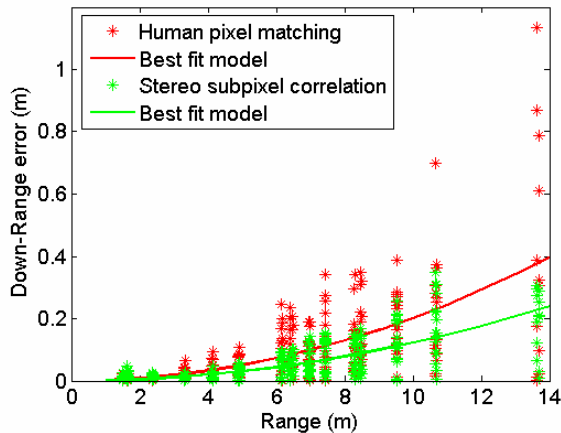


Figure 22. Down-range error

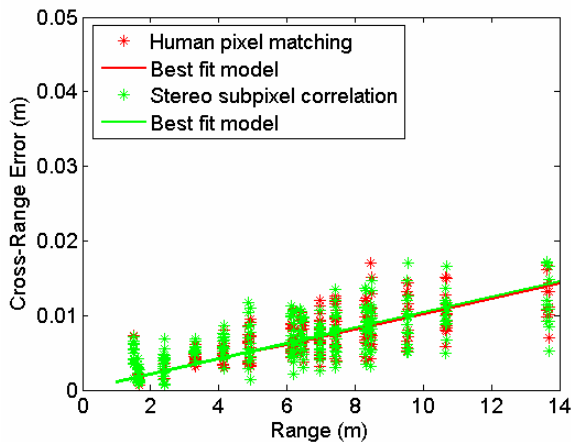


Figure 23. Cross-range error

6 Conclusions

In this paper, we presented our findings on the performance and error analysis of the JPL stereo system. Also the stereo localization errors were validated experimentally. The results are applicable to any similar real-time correlation based stereo technique.

Acknowledgment

This work was performed at the Jet Propulsion Laboratory, California Institute of Technology, under a contract with the National Aeronautics and Space Administration. This work is supported by NASA Mars Science Laboratory (MSL) Focused Technology Program.

References

- [1] D. Scharstein and R. Szeliski, "A Taxonomy and Evaluation of Dense Two-Frame Stereo Correspondence Algorithms," *Int. J. Computer Vision*, vol. 47, pp.7-42, 2002.
- [2] <http://iris.usc.edu/Vision-Notes/bibliography/contents/stereo.html>
- [3] S. B. Goldberg, M.W. Maimone, L. Matthies, "Stereo Vision and Rover Navigation Software for Planetary Exploration," *IEEE Aerospace Conf.*, Mar. 2002.
- [4] Y. Xiong, L. Matthies, "Error analysis of a real-time stereo system". *IEEE Conference on Computer Vision and Pattern Recognition (CVPR)*, San Juan, Puerto Rico, June 1997.
- [5] R. Volpe, I.A.D. Nesnas, T. Estlin, D. Mutz, R. Petras, H. Das, "CLARAty: Coupled Layer Architecture for Robotic Autonomy." *JPL Technical Report D-19975*, Dec 2000.
- [6] A. Ansar and W. Kim, Mars Science Laboratory Technology Functional Design Document: Stereo Vision, *JPL Internal Document*, June 2003.
- [7] W. Kim, R. Steinke, R. Steele, and A. Ansar, Camera Calibration and Stereo Vision Technology Validation Report, *JPL D-27015*, Jan. 2004.
- [8] W. Kim, A. Ansar, R. Steele, "Rover Mast Calibration, Exact Camera Pointing, and Camera Handoff for Visual Target Tracking," to appear in *Int. Conf. on Automation and Robotics (ICAR)*, July 2005.